

Hydrothermal Synthesis of Ce/Zr co-substituted BiFeO₃: R3c-to-P4mm Phase Transition and Enhanced Room Temperature Ferromagnetism

Zahra Adineh

Damghan University

Ahmad Gholizadeh (✉ gholizadeh@du.ac.ir)

Damghan University <https://orcid.org/0000-0003-2377-6808>

Research Article

Keywords: Bismuth ferrite, Hydrothermal method, Structural transition, Raman spectroscopy, Magnetic transition

Posted Date: March 17th, 2021

DOI: <https://doi.org/10.21203/rs.3.rs-304914/v1>

License:  This work is licensed under a Creative Commons Attribution 4.0 International License.

[Read Full License](#)

Hydrothermal synthesis of Ce/Zr co-substituted BiFeO₃: *R3c*-to-*P4mm* phase transition and enhanced room temperature ferromagnetism

Zahra Adineh; Ahmad Gholizadeh*

School of Physics, Damghan University, Damghan, Iran

Abstract

A facile hydrothermal method was used for fabricating phase-pure Bi_{1-x}Ce_xFe_{1-x}Zr_xO₃ ($x = 0.00, 0.03, 0.06$) multiferroic ferrites, and the dependence of structural, optical, and magnetic properties on the composition have been investigated. The samples were investigated by X-ray diffraction (XRD), Raman and Fourier-transform infrared (FT-IR) spectroscopies, scanning electron microscopy, UV-Vis spectroscopy, and vibrating sample magnetometer at room temperature. Structural results show that the structure of Bi_{1-x}Ce_xFe_{1-x}Zr_xO₃ ferrites is indexed to a rhombohedral structure with *R3c* space group. However, the weakening in the intensity, the expansion of the line-width of all bands, and some band shifts observed in Raman spectra indicate a structural transition from rhombohedral (*R3c*) to pseudo-tetragonal (*P4mm*) phase as the content of Ce/Zr increases. Also, a significantly enhanced intensity of the A1-2 mode in Raman spectra means that there is a novel behavior of magnetic anisotropy in the Ce/Zr co-substituted samples. A significant increase in optical band gap with increasing of the Ce/Zr co-substitution suggests that the materials are suitable for technological applications. Magnetic properties of the samples show a magnetic transition from antiferromagnetic to ferromagnetic phase due to the presence of the rhombohedral to the tetragonal phase transition, and exchange interaction between the 4f orbitals of the Ce³⁺/Ce⁴⁺ and the 3d orbitals of the Fe³⁺/Fe²⁺.

Keywords: Bismuth ferrite; Hydrothermal method; Structural transition; Raman spectroscopy; Magnetic transition.

*Corresponding author, Tel-Fax: +982335220090; e-mail address: gholizadeh@du.ac.ir; ah_gh1359@yahoo.com

1. Introduction

BiFeO₃(BFO) is the most famous multiferroic material having the antiferromagnetic Néel temperature (= 370 K) and the ferroelectric Curie temperature (= 830 K) which simultaneously shows a saturation polarization and magnetic moment of 90 $\mu\text{C}/\text{cm}^3$ and 8-9 emu/cm^3 , respectively [1]. The ferroelectricity and G-type antiferromagnetic characteristics of BFO come respectively from the lone-pair distortion on the 6s² of Bi³⁺ ions and spin-exchange coupling between half-filled 'd' orbital of Fe³⁺ ions [2-3]. Despite this, inherent problems of the bulk BFO such as formation of secondary phases, high leakage current, low magnetoelectric (ME) coupling, zero macroscopic remnant magnetization (M_r) have been restricted its multifunctional applications at room temperature [4-7]. In recent years, attempts have been made to enhance reduce dielectric loss, ferroelectric properties, and leakage current, increase remnant polarization, modify its inhomogeneous-spatial spin-modulated (incommensurate) structure, and intensify magnetoelectric interaction [8-21]. However, the comparative studies were undertaken in order to understand of the effect of co-substitution at A- and B-site on ferroelectric and magnetic properties, respectively. Recent studies revealed that a strategy of co-doping of the Bi-site, and Fe-site can significantly improve the magnetic and ferroelectric properties of BFO nanoparticles, [11-21]. We recently reported that the A-site (Nd, Y, Gd) and B-site (Mn, Zr) co-substitution of BFO have a result to reduce the particle size to less than 62 nm which will destruct or suppress the magnetic spiral structure [6-7]. However, in present work, hydrothermal method was used for the synthesis of pure single-phase Bi_{1-x}Ce_xFe_{1-x}Zr_xO₃ ($x = 0.00, 0.03, 0.06$) at a low temperature 180 °C without a further calcination step. Also, we selected Ce substitution, because $r_{\text{Ce}^{3+}}(\text{CN}: 12) = 1.34 \text{ \AA}$ is closer to the $r_{\text{Bi}^{3+}}(\text{CN}: 12) (1.4 \text{ \AA}, 6s \text{ lone pair})$ so that it results in a low symmetry distorted rhombohedral structure with $R3c$ space group accompanied by a large

polarization along the hexagonal [001] or the pseudocubic [111] direction [21-23]. Furthermore, it highly expects that Bi³⁺ substitution with Ce³⁺ can reduce the leakage current density accompanied by a further improvement in the ferroelectric properties of BFO [23]. However, Ce³⁺ substitution act as a donor in oxygen octahedron and helps to reduce the oxygen vacancies by restricting the formation of Fe³⁺ to Fe²⁺ ions [21]. Previous reports on Zr⁴⁺ substitution for Fe³⁺ showed that lattice strains and defects originated from a mismatch in ionic radii prevents the growth of the grain sizes as the substitution increases and all the samples show the antiferromagnetic behavior [24]. While in A/Zr co-substitution for Bi/Fe, the particle sizes goes down and a weak ferromagnetic behavior with an improvement of microwaves properties are observed [7, 25]. Detailed studies of structural, optical, and magnetic properties indicate novel behaviors of the pure single-phase Bi_{1-x}Ce_xFe_{1-x}Zr_xO₃ (x = 0.00, 0.03, 0.06) hydrothermally synthesized with improved magnetic properties.

2. Experimental

2.1. Preparation of Bi_{1-x}Ce_xFe_{1-x}Zr_xO₃

To prepare the Bi_{1-x}Ce_xFe_{1-x}Zr_xO₃ (x = 0.00, 0.03, 0.06) nanoparticles by hydrothermal method, first, a solution of initial material nitrates with appropriate moles under continuous stirring is obtained. The Bi(NO₃)₃.5H₂O is dissolved in 5 mL concentrated HNO₃ and then all ZrO(NO₃)₂.H₂O, Ce(NO₃)₃.6H₂O, and Fe(NO₃)₃.9H₂O were separately dissolved in 5 mL of distilled water. After that, all the precursors were mixed under continuous magnetic stirring to obtain a completely clear solution. Then, 40 g of KOH solution was dropwise added to the above solution and then the mixture was poured into a Teflon-lined stainless steel autoclave for the

hydrothermal treatment at 180 °C for 6 h. The precipitate was filtered and washed with distilled water to remove $(\text{NO}_3)^{-1}$ and K^+ ions. Next, the resulted precipitate was dried in an oven at 110 °C for 3 h. To ensure accurate and reproducible results, the high purity reagents and chemicals were used which were purchased from Sigma-Aldrich.

The crystal phase of the $\text{Bi}_{1-x}\text{Ce}_x\text{Fe}_{1-x}\text{Zr}_x\text{O}_3$ ($x = 0.00, 0.03, 0.06$) nanoparticles was identified by powder X-ray diffraction (XRD, D8-Advance Bruker AXS diffractometer) with a $\text{Cu-K}\alpha$ radiation ($\lambda = 1.54048 \text{ \AA}$). The patterns were analyzed by using the Fullprof program. Raman spectra were performed in a Renishaw 1000 confocal Raman microscope using a 532 nm diode-pumped solid-state laser (Cobolt) with a laser power of 10 mW. The Fourier transform infrared (FTIR) spectra of the samples were obtained from a Perkin-Elmer FT-IR spectrometer. The surface morphology images of the samples were recorded by field-emission scanning electron microscopy (FESEM, HITACHI S-4160 model). The absorption spectra of the samples were recorded by a UV-Vis system (Agilent8453, Palo Alto, CA). The direct-transition bandgap energy of the samples was estimated through Tauc's equation [26]. The hysteresis loops of the samples were recorded using the VSM 7407 Lake Shore's vibrating sample magnetometer at room temperature and a maximum magnetic field of 2T.

3. Results and discussion

3.1. Structural analysis

Fig. 1(a) shows XRD patterns of a single-phase perovskite structure of $\text{Bi}_{1-x}\text{Ce}_x\text{Fe}_{1-x}\text{Zr}_x\text{O}_3$ ($x = 0.00, 0.03, 0.06$) nanoparticles. It reveals the presence of a rhombohedral crystal structure with $R3c$ space group for BFO which is in accordance with the JCPDS card (no. 86-1518) [7]. After

Ce³⁺/Zr⁴⁺ ions doping into BFO, the doublet diffraction peaks (104) and (110), (006) and (202), (116) and (112), (118) and (300) of the rhombohedral structure are merging to the singlet peak as shown in Fig. 1. Also, the location of all the diffraction peaks shifted toward a higher angle.

Although the intensity of XRD peaks located at the higher angles is increasing, the intensity of singlet peak (012)_R at about 22° becomes smaller. Besides, an enlarged view of (012)_R and (024)_R reflections is plotted inset of Fig. 1 to show the structural change as Ce³⁺/Zr⁴⁺ content increases up to $x = 0.06$. As seen from Fig. 1, a splitting in both the parallel (012)_R and (024)_R reflections of the rhombohedral structure which are singlet peaks, occur with the addition of Ce³⁺/Zr⁴⁺ content. The singlet (012)_R peak is split into two sub-peaks, a larger peak at about 22.50° and a smaller peak at about 22.75° which are respectively corresponded to the reflection planes (001)_T and (100)_T of tetragonal structure. Similarly, the singlet (024)_R peak is split into two sub-peaks, a larger peak at about 45.90° and a smaller peak at about 46.40° which are respectively corresponded to the reflection planes (002)_T and (200)_T of the tetragonal structure. It should be noted that the intensity of the (001)_T and (002)_T reflections of the tetragonal structure is smaller than the (100)_T and (200)_T, respectively [27]. Since the structure of sample $x = 0.06$ is a mixture of the tetragonal (*P4mm*) and rhombohedral (*R3c*) phases, the peak overlap of the (012)_R with the (001)_T and the peak overlap of the (024)_R with the (002)_T occurs. These findings could be related to the fact that the lower-symmetry rhombohedral structure of BFO gradually transforms into a higher-symmetry tetragonal structure due to the changes of bond lengths Bi-O and Fe-O after the Ce³⁺/Zr⁴⁺ doping into BFO, which is discussed further below.

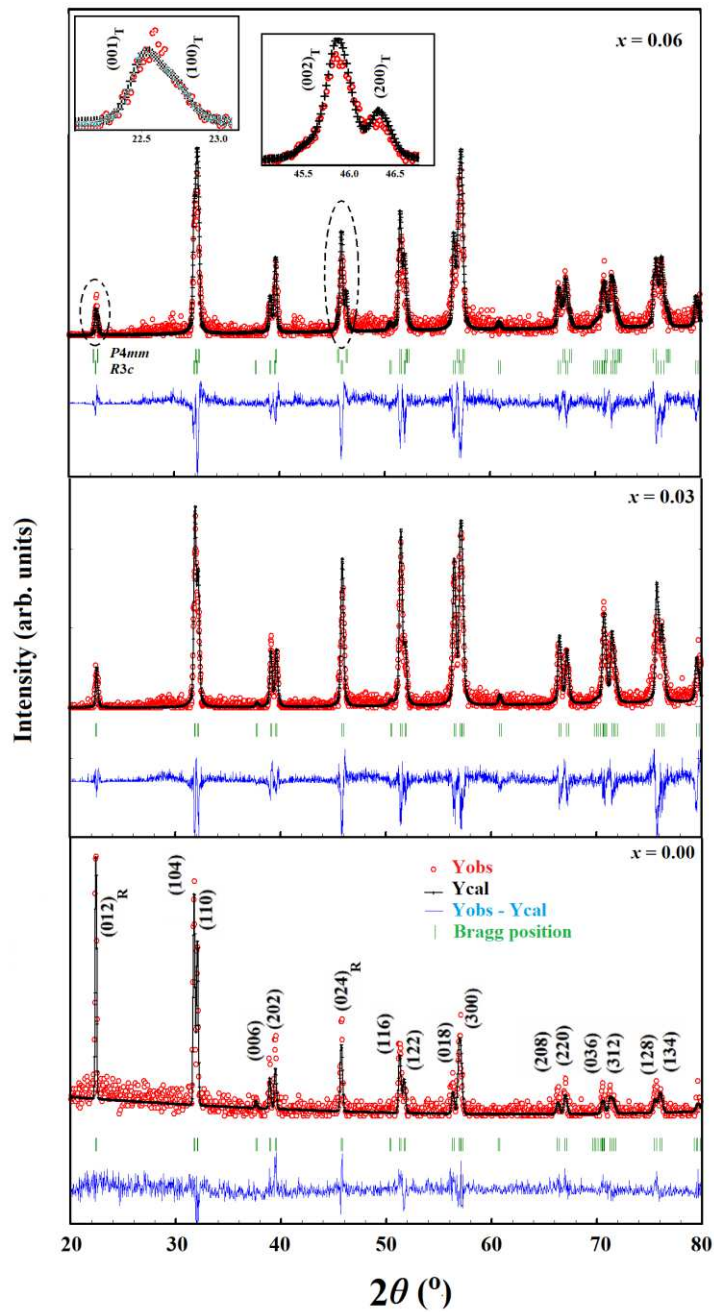


Fig. 1 XRD pattern and Rietveld analysis with rhombohedral (space group $R3c$) structural model for $\text{Bi}_{1-x}\text{Ce}_x\text{Fe}_{1-x}\text{Zr}_x\text{O}_3$ ($x = 0.00, 0.03$) and a mixed-phase tetragonal ($P4mm$) + rhombohedral ($R3c$) structural models for $x = 0.06$. Red circles and black solid lines represent the raw data and the calculated profile, respectively. Green vertical lines indicate the position of Bragg peaks for rhombohedral structure. The blue lower trace shows the difference between the observed (the raw data) and the calculated patterns.

Table 1 The lattice parameters of conventional hexagonal (a_H , c_H), primitive rhombohedral (a_R , α_R) structures, crystallite size (D_{W-H}) and microstrain (ε) obtained from the Williamson-Hall method for $\text{Bi}_{1-x}\text{Ce}_x\text{Fe}_{1-x}\text{Zr}_x\text{O}_3$.

sample	$x = 0.00$	$x = 0.03$	$x = 0.06$	
			<i>rhombohedral</i>	<i>Tetragonal</i>
$a_H = b_H$ (Å)	5.5849	5.5691	5.5691	3.9193
c_H (Å)	13.8791	13.8384	13.8252	3.9832
$a_R = b_R = c_R$ (Å)	5.6394	5.6228	5.6185	---
$\alpha_R = \beta_R = \gamma_R$ (°)	59.360	59.369	59.391	90
$V_R = V_H/3$ (Å ³)	124.971	123.901	123.676	61.185
D_{W-H} (nm)	82.27	28.78	28.78	
ε (no unit)	+0.00113	-5.315E-4	-5.318E-4	

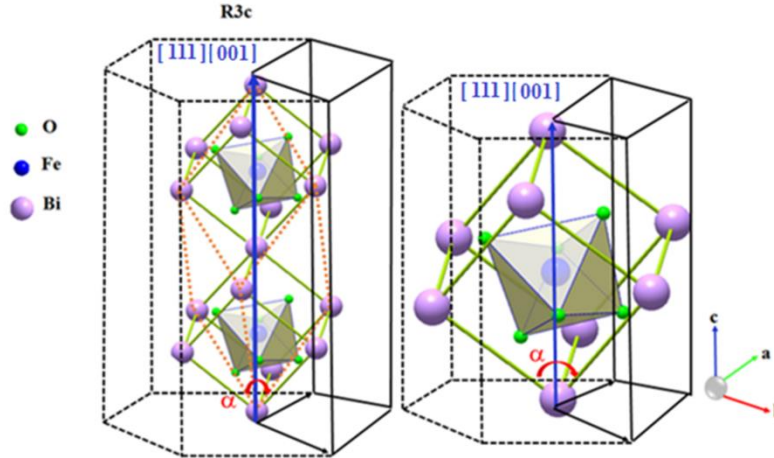


Fig. 2 Left panel is a scheme of the relationship between the primitive rhombohedral (dashed, red), cubic (solid, green), and hexagonal cells of bulk BFO. The right panel is half of the left panel. Here, [001] crystallographic axis of the hexagonal structure is parallel to the [111] axis of the rhombohedral or the cubic structures.

The Rietveld refinement of the XRD patterns of the samples using Fullprof software confirms the formation of the rhombohedral structure with $R3c$ space group (see Fig. 1) and refined lattice parameters listed in Tables 1. Primitive rhombohedral and hexagonal structures in a stable perovskite structure of BiFeO_3 are shown in Fig. 2. The values of the ion radius of the cations used in this work which located at the six-fold coordination site (octahedron site) and the twelve-fold coordination site (dodecahedral site), are as follow: $r_{\text{Ce}^{3+}}(\text{CN}:12) = 1.34 \text{ \AA}$, $r_{\text{Ce}^{4+}}(\text{CN}:12) = 1.14 \text{ \AA}$, $r_{\text{Bi}^{3+}}(\text{CN}:12) = 1.4 \text{ \AA}$, $r_{\text{Fe}^{3+}}(\text{CN}:6) = 0.645 \text{ \AA}$, $r_{\text{Zr}^{4+}}(\text{CN}:6) = 0.72 \text{ \AA}$ [28-29]. According to these values, substituting the smaller Ce^{3+} for larger Bi^{3+} , will reduce the unit cell volume. Simultaneously, it is expected that Zr^{4+} replacement instead of Fe^{3+} will increase the unit cell volume. For better discussion, we calculated the difference in ion radii of the host ions with the substituted ions as follows:

$$r_{\text{Ce}^{3+}} - r_{\text{Bi}^{3+}} = -0.06 \text{ \AA} \quad , \quad r_{\text{Zr}^{4+}} - r_{\text{Fe}^{3+}} = +0.075 \text{ \AA}$$

Therefore, it is expected that the lattice volume will increase with the $\text{Ce}^{3+}/\text{Zr}^{4+}$ co-substitution in BFO. However, a shift of the XRD peaks to the larger angles with an accompanying decrease of the lattice volume suggests the presence of various cations of Ce^{3+} and Ce^{4+} in the samples (see Table 1). It should be noted that it is harder to enter the Zr^{4+} ions having an ionic radius larger than Fe^{3+} , which may results in oxidation of Ce^{3+} to Ce^{4+} . Since the electronic configuration of Ce is $4f^1 5d^1 6s^2$ (atomic number of 58), one among the lanthanides, Ce^{3+} ions having the configuration $4f^1 5d^0 6s^0$ can easily lose an electron to acquire the configuration $4f^0$ and attains the stable configuration of Xenon. Here, oxidation of Ce^{3+} ($\text{Ce}^{3+} \rightarrow \text{Ce}^{4+} + e^-$), and reduction of Fe^{3+} ($\text{Fe}^{3+} + e^- \rightleftharpoons \text{Fe}^{2+}$, for the presence of charge neutralization) occur with increase of Ce/Zr co-substitution, then the oxidation of iron(III) ions by cerium(III) ions results in following relation: $\text{Ce}^{3+} + \text{Fe}^{3+} \rightleftharpoons \text{Ce}^{4+} + \text{Fe}^{2+}$.

The increase in the angle of α_R near to 60° and decreasing of the lattice parameters given in Table 1 with the doping amount of $(\text{Ce}^{3+}\text{-Ce}^{4+})/\text{Zr}^{4+}$ ions indicates a slight contraction of the FeO_6 octahedral along the body diagonal [111] of rhombohedral (111) axis (c axis of hexagonal) or the c -axis [001], which is accompanied with a transition to a higher symmetry structure (see Fig. 2) [6-7].

In the Williamson-Hall (W-H) method (Fig. 3), the $\beta \cos \theta$ (y -axis) plot versus $4 \sin \theta$ (x -axis) corresponding to the three parallel reflection planes (012), (024), (036) has a positive slope for BFO, while it indicates a negative slope for Ce/Zr co-substituted BFO. The crystallite size (D) is calculated by the inverse of the y -intercept of linearly fitted data and microstrain (ε) is obtained from the slope [30]. The results of Table 1 show the remarkable changes in the crystallite size and the microstrain contribution from the broaden X-ray profile for the Ce/Zr co-substituted BFO. With the increase of the Ce/Zr co-substitution in BFO, the value of the D decrease and the ε become negative due to the presence of compressive stress. This compressive stress created into the BFO lattice can be related to the ionic radii mismatch between $\text{Ce}^{3+}/\text{Ce}^{4+}$ and Zr^{4+} ions with the Bi^{3+} and Fe^{3+} , respectively.

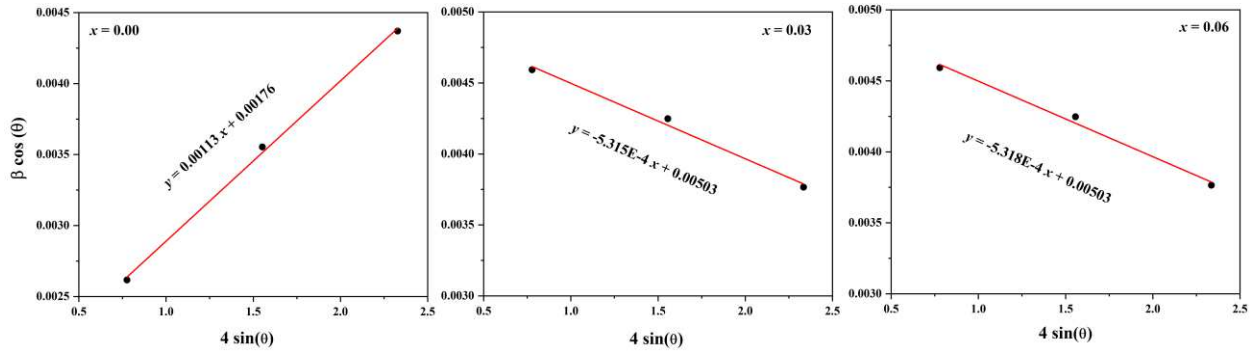


Fig. 3 Williamson-Hall plots of $\text{Bi}_{1-x}\text{Ce}_x\text{Fe}_{1-x}\text{Zr}_x\text{O}_3$.

3.2 Raman and FTIR spectroscopies

Many reasons are indicating that the local structure analysis of substituted BFO nanoparticles can be explained more clearly by the IR and Raman spectroscopies: 1-The structural analysis of BFO nanoparticles by XRD is hampered by the reflection broadening so that splitting the XRD peaks of BFO just covered by the broadening [6]. 2- In particular, the presence of Fe in combination with Cu- $K\alpha$ radiation leads to significant X-ray fluorescence and high measurement backgrounds [30]. These easily can cover the presence of low-level impurities.

Fig. 4(a) shows the Raman spectra measured at room temperature for $\text{Bi}_{1-x}\text{Ce}_x\text{Fe}_{1-x}\text{Zr}_x\text{O}_3$. According to group theory, distorted rhombohedral BiFeO_3 have 18 optical vibration modes (= $4A_1+5A_2+9E$), which A_1 (TO) and E (LO) are Raman and infrared active vibration modes, respectively, and $5A_2$ are Raman inactive vibration modes. So, the 13-point Raman active phonons (= $4A_1+9E$) of distorted rhombohedral perovskite structure ($R3c$ space group) can propagate in longitudinal and transverse directions as following [31]: Four A_1 modes propagating along the c -direction, A_1-1 , A_1-2 , A_1-3 , and A_1-4 and nine E modes propagating along the x - y plane. Generally, the A_1-1 and A_1-2 modes show strong scattering intensities, whereas the A_1-3 , and A_1-4 modes show weak scattering intensities [32-37]. By comparison, the scattering intensity of nine E modes is medium. However, the resonance frequency and the shape of the spectral line depend on the characteristics of the samples. According to previous reports [32-35], the polar phonon modes of A_1-1 , A_1-2 , and E_1 are mainly contributed to spin-phonon coupling, magnetic anisotropy, and magnetoelectric coupling, respectively. In this research, a slight shift of the A_1-1 , A_1-2 , and A_1-3 modes (assigned to the Bi-O bonds) to higher

frequencies and a significant change in their intensities with the increase of the Ce and Zr co-substitution indicate that the Ce^{4+} ions of smaller size are substituted for the Bi^{3+} ions. Fig. 5 shows two strong peaks near 132, and 168 cm^{-1} assigned to the A1-1, and A1-2 phonon modes and two weak peaks at 224, and 426 cm^{-1} assigned to A1-3, and A1-4 phonon modes. Also, the Raman spectra indicate a significant decrease in the scattering intensity of A1-1 mode and an obvious increase in the scattering intensity of A1-2 mode as the Ce/Zr co-substitution increase. The relatively reduced intensity of the A1-1 mode with the degree of the Ce/Zr co-substitution indicates a decrease in the spin-phonon coupling. The relatively enhanced intensity of A1-2 Raman mode with increasing the Ce/Zr co-substitution in BFO indicates that two predominant scattering mechanisms controlling the magnetic anisotropy are the spin-dependent and spin-phonon scattering, so that the Raman intensity of a magnetically ordered phase can be expressed as $I = |R + M\langle S_i S_j \rangle / S^2|^2$. Here, R and M are the spin-independent, and the magnetic moment parameters, respectively, and $S_i S_j / S^2$ is the nearest-neighbor spin-spin correlation function. The increase in the intensity of A1-2 mode is due to different contributions from the correlation function $S_i S_j / S^2$, in different directions, which is the result of a change in the magnetic ordering due to the spin-reorientation phase transitions. According to our structural results, it may be attributed to the presence of $(001)_T$ and $(002)_T$ peaks oriented in the c-axis direction of the Ce/Zr co-substituted BFO.

The positions of all the observed Raman peaks for samples $\text{Bi}_{1-x}\text{Ce}_x\text{Fe}_{1-x}\text{Zr}_x\text{O}_3$ are given in Table 2. The atomic mass also plays a very important role in a harmonic vibrating system ($\omega = \sqrt{\frac{k}{m}}$). The molar mass of Fe^{3+} , Zr^{4+} , Bi^{3+} , Ce^{3+} , and Ce^{4+} , are 55.845, 91.22, 208.979, 140.114, and 139.905 g/mol, respectively. The molar mass of the Ce^{3+} , and Ce^{4+} are less than

that of the Bi^{3+} . Nevertheless, at a replacement of less than 15%, the calculated average molar mass does not have much effect [36].

The Raman spectra (Fig. 4(c)-(d)) show remarkable changes in some band shifts, the expansion of the line-width of all bands, and the weakening in the intensity of the BFO structure with the increases of Ce/Zr content. It indicates an intensity change in A_1 modes and the shift in the E modes. As seen, the intensity of the A_1 -1 mode decreases, while A_1 -2 phonons increases after Ce/Zr ions are incorporated. When, Ce/Zr co-substitution increases up to 0.06, E_4 mode at 299 cm^{-1} shifts to a lower wavenumber, followed by merging with the phonon mode E_3 at 263 cm^{-1} . At the same time, the E_7 mode at 471 cm^{-1} shifts to a higher wavenumber, followed by merging with the phonon mode E_8 at 518 cm^{-1} . According to our structural results, an increase in the intensity of the E_7 mode may be attributed to the presence of peaks $(100)_T$ and $(200)_T$ oriented in an a -axis direction in the Ce/Zr co-substituted BFO. Also, the E_5 and E_6 modes at 343 and 367 cm^{-1} , respectively, become gradually weak and finally disappear. On the other hand, the mean radius of the $\text{Ce}^{3+}/\text{Ce}^{4+}$ ions is smaller than that of the Bi^{3+} ions, which a decrease in d spacing yields a compressive force into the A-sites of the BFO lattice as seen from Fig. 3. These results indicate a structural transition from a rhombohedral structure to a higher-symmetry pseudo-tetragonal, in agreement with our XRD results. When the induced microstrain by the Ce/Zr co-substitution causes the BFO structure to transit to tetragonal ($P4mm$ space group), the Raman active modes can be expressed by the following irreducible representation: $3A_1+B_1+4E$ [37].

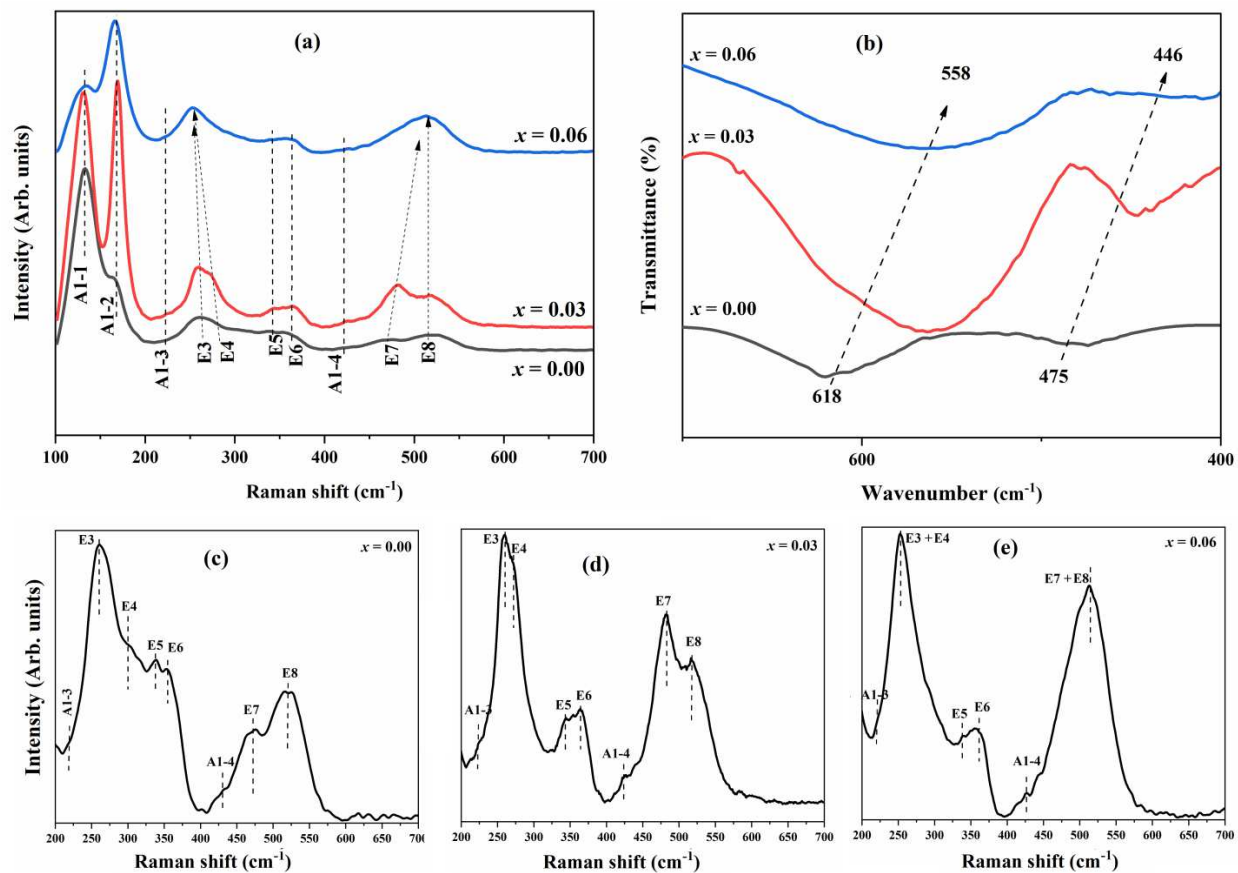


Fig. 4 (a) Raman spectra (b) FT-IR spectra of $\text{Bi}_{1-x}\text{Ce}_x\text{Fe}_{1-x}\text{Zr}_x\text{O}_3$. Selected enlarged region (200–700 cm^{-1}) of samples (c) $x = 0.00$, (d) $x = 0.03$, (e) $x = 0.06$.

Table 2 Raman peak positions for samples $\text{Bi}_{1-x}\text{Ce}_x\text{Fe}_{1-x}\text{Zr}_x\text{O}_3$. The unit is cm^{-1} .

Raman modes (cm^{-1})	$x = 0.00$	$x = 0.03$	$x = 0.06$
A1-1	132	136	136
A1-2	163	167	169
A1-3	218	224	223
A1-4	428	428	428
E3	260	259	252
E4	299	270	256
E5	337	341	341
E6	353	363	363
E7	471	482	513
E8	518	518	518

Fig. 4(b) shows FT-IR spectrum of $\text{Bi}_{1-x}\text{Ce}_x\text{Fe}_{1-x}\text{Zr}_x\text{O}_3$ ($x = 0.00, 0.03, 0.06$). It is known that the absorption frequencies observed in the range of 400 to 700 cm^{-1} are related to metal-oxygen vibrations of the perovskite structure [38-40]. The strong absorption frequencies found at wavenumbers 475 and 618 cm^{-1} of the BFO are related to the asymmetric bending and the symmetric stretching vibrations of the iron-oxygen bond in the FeO_6 octahedral iron sites. The former frequency only appears in the high-distortion rhombohedral structure of the perovskite oxides [40]. As seen from Fig. 4(b), there is no absorption peak at about 446 cm^{-1} for $x = 0.06$, indicating which a structural phase transition from $R3c$ low-symmetry rhombohedral structure to $P4mm$ high-symmetry tetragonal structure occurs as obtained from XRD and Raman analysis. However, we can observe that the position of absorption peak located at 618 cm^{-1} shifts to a lower wavenumber located at 558 cm^{-1} , indicating success substitution of the Fe^{3+} ion by bigger Zr^{4+} ion.

3.3 Morphological analysis

Fig. 5 shows FESEM images for the $\text{Bi}_{1-x}\text{Ce}_x\text{Fe}_{1-x}\text{Zr}_x\text{O}_3$ ($x = 0.00, 0.06$) on a scale of 500 nm and 1 μm . The images show the effect of the Ce/Zr co-substitution on the morphology of BFO. The observed micro-and nano-size grains of BFO has a hexagonal basal plane with a nonhomogeneous distribution. It is clear that Ce/Zr co-substitution increases the grain size and the platelet hexagons show lower porosity and higher density than that for BFO. According to the structure results, further reduction in the internal microstrain with increasing the Ce/Zr co-substitution accompanied by a reduction in internal energy and pressure can only be achieved by a decrease of the grain boundary or increase of the grain size [7].

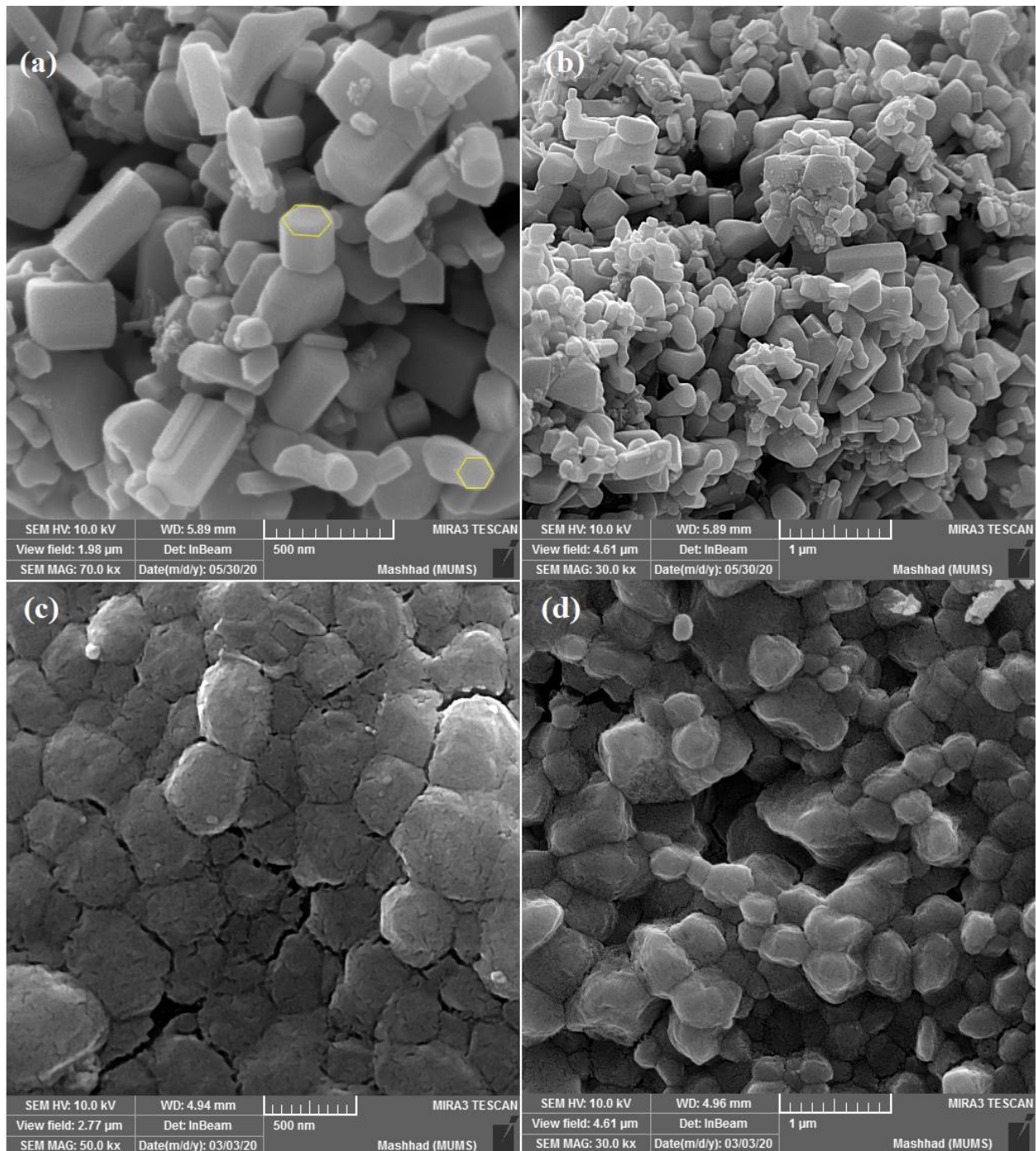


Fig. 5 FE-SEM images for (a), (b) $x = 0.00$, and (c), (d) $x = 0.06$ on a scale of 500 nm and 1 μm .

3.4 Optical characterization

Fig. 6 shows Tauc plots of $(\alpha h\nu)^2$ versus the photon energy ($h\nu$) of $\text{Bi}_{1-x}\text{Ce}_x\text{Fe}_{1-x}\text{Zr}_x\text{O}_3$ ($x = 0.00, 0.03, 0.06$). The direct energy gap has been calculated from the extrapolating of the linear part of the plots, as shown in Fig. 6. The bandgap energy of BFO ($=2.04$ eV) is related to the electronic charge transfer from O 2p states (valence band) to Fe 3d states (conduction band) which has significantly increased with Ce/Zr co-substitution.

Zhou et al. [41] have reported an increase in optical band gap in Sm and Mn co-doped BFO which may be due to Burstein–Moss effect. A similar increase in optical band gap is also reported for Y and Co co-doping of BFO due to a decrease in the density of state in the valence band [42]. However, there are contradictory reports on the effect of Ce substitution on the bandgap energy of BFO [43-45]. Here, the increase of the gap energy cannot be originated the quantum confinement phenomenon (see the SEM images). It can be attributed to the following reasons: (1) the synergetic effect of Ce and Zr co-substitution on the band structure of BFO is due to the change of the Fe-O and the Bi-O length bonds and the Fe-O-Fe bond angles which may cause a decrease in the density of state in the valence band. (2) According to Burstein–Moss effect, some states close to the conduction band being populated which would result in a blue shift of the optical bandgap, with increasing Ce content (Ce acts as a donor) [7, 41-45]. These will lead to a shift in the fundamental absorption edge towards higher photon energy. A significant increase in optical bandgap energy with increasing of the Ce/Zr co-substitution suggests that the materials are suitable as UV and blue-green-driven photocatalysts, or for optoelectronic devices.

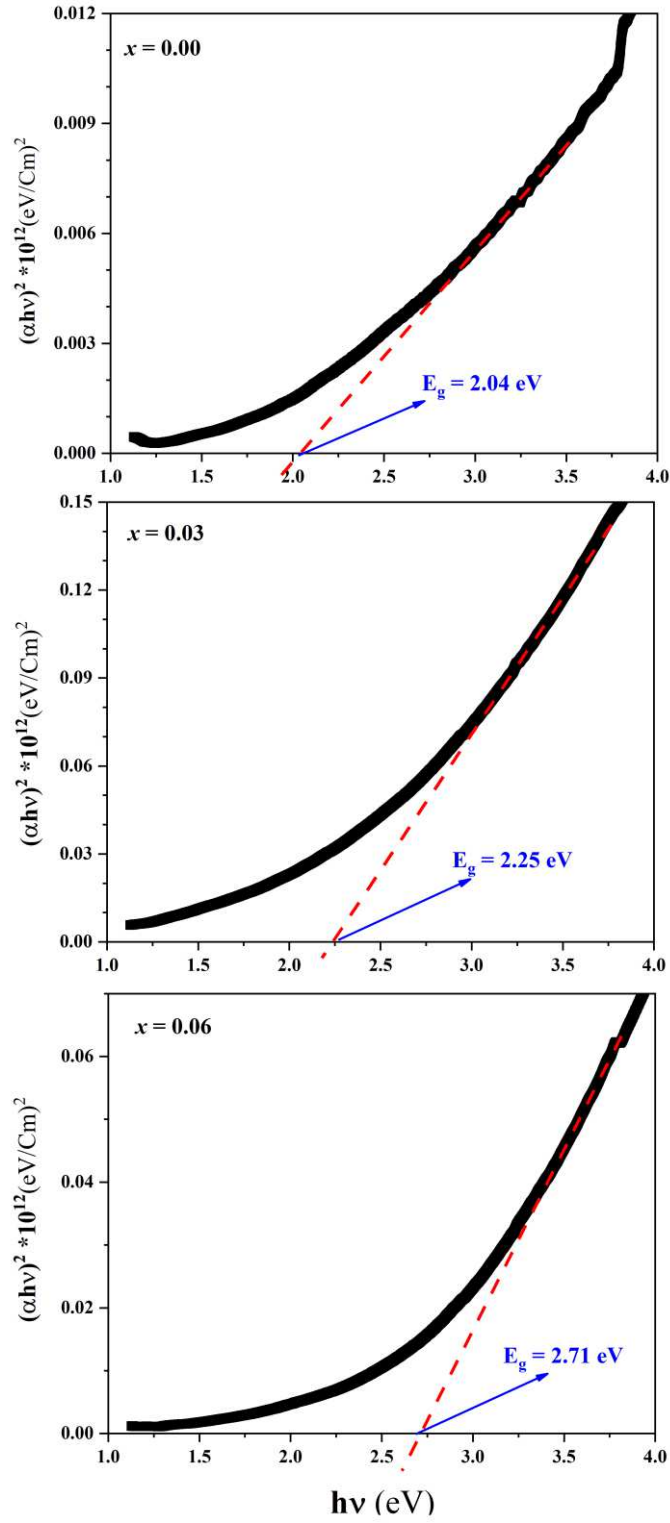


Fig. 6 Plots of $(\alpha hv)^2$ vs. $h\nu$ for the samples.

3.5. Magnetic measurements

The room-temperature magnetization curves of $\text{Bi}_{1-x}\text{Ce}_x\text{Fe}_{1-x}\text{Zr}_x\text{O}_3$ ($x = 0.00, 0.03, 0.06$) are shown in Fig. 7. From the curves, we can extract the highest field magnetization (M_H), coercive field (H_c), magnetization at zero applied fields (M_r , the remanent magnetization) for the samples as listed in Table 3.

According to the law of approach to saturation (LAS), anisotropy constant can be calculated by fitting the magnetization curves at the high sufficiently field regions ($H \gg H_c$) with relation (see Fig. 8): $M(H) = M_s \left(1 - \frac{a}{H} - \frac{b}{H^2}\right) + \chi H$, where $M(H)$ is the magnetization at the applied field H [46-48]. Also, the parameters M_s , a , b , and χ are saturation magnetization, inhomogeneity parameter, factor proportional K_1^2 (K_1 anisotropy constant), and susceptibility, respectively. They are obtained from the fitting method and listed in Table 3. According to our structural results, the Fe^{3+} ion extracts an electron from Ce^{3+} to form Ce^{4+} and Fe^{2+} ions. However, the Fe^{2+} ion contributes to anisotropy, but the Fe^{3+} ion is expected to be isotropic based on their electron structure. Finally, the increase in the coercive field in Ce/Zr-substituted samples with the substitution has been attributed to the increase of the $\text{Fe}^{2+}/\text{Fe}^{3+}$ ratio and K_1 anisotropy constant.

An almost linear increase and small values of the magnetization curves indicate the antiferromagnetic nature of sample BFO which is changed to the weak ferromagnetic as Ce/Zr co-substitution increase (see Fig. 8). However, the presence of the paramagnetic nanoparticles or high magnetic anisotropy of the samples causes the magnetization curves to do not saturate even in the highest applied fields [7, 48]. The increase of M_r and M_H with the Ce/Zr substitution can be related to two reasons: First, a mixture of the rhombohedral and tetragonal

structural phases can destroy the spiral spin modulation with an increase of the magnetization [6-7, 49-50]. Second, when magnetic ion Ce^{3+} having a large magnetic moment of $2.4 \mu_B$ substitutes for nonmagnetic ion Bi^{3+} , an exchange interaction between 3d orbital of Fe^{3+} ion and 4f orbital of Ce^{3+} ion at the B- and A-sites, respectively, produce a local ferrimagnetic spin configuration accompanied by a magnetic enhancement [51].

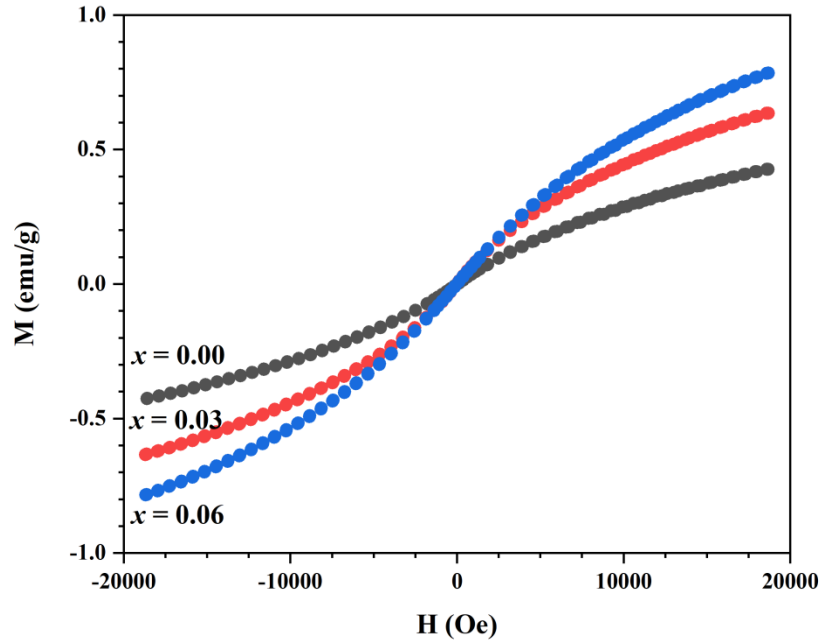


Fig. 7 Magnetization curve measured at 300 K for $\text{Bi}_{1-x}\text{Ce}_x\text{Fe}_{1-x}\text{Zr}_x\text{O}_3$.

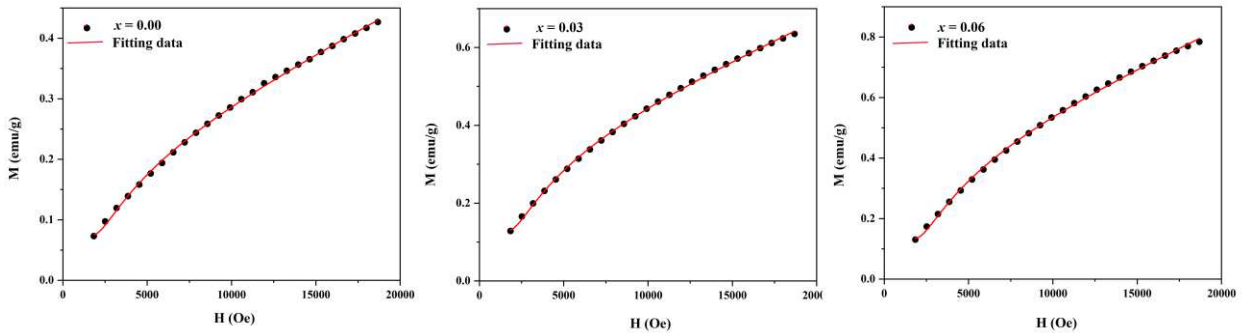


Fig. 8 LAS curves for $\text{Bi}_{1-x}\text{Ce}_x\text{Fe}_{1-x}\text{Zr}_x\text{O}_3$.

Table 3 The values of remanent magnetization (M_r), coercivity (H_c), and magnetization at the highest applied field (M_H) and the fitting parameters of LAS curve ($M = M_s(1-a/H-b/H^2)+\chi H$) for $\text{Bi}_{1-x}\text{Ce}_x\text{Fe}_{1-x}\text{Zr}_x\text{O}_3$.

Sample	H_c (Oe)	M_H (emu/g) at 2T	M_r (emu/g)	a (Oe)	$b \cdot 10^{-6}$ (Oe ²)	$\chi \cdot 10^5$ (emu/Oe)
$x = 0.00$	2.56	0.427	0.96 E-4	2975.78	2.93	1.38
$x = 0.03$	6.50	0.634	5.23 E-4	2738.87	2.62	1.86
$x = 0.06$	7.10	0.784	5.31 E-4	3154.20	3.18	2.41

4. Summary

We have summarized the key points from our work on the Ce/Zr co-substituted BFO as follows:

(1) the XRD and Raman spectroscopy results indicate a rhombohedral-tetragonal phase structural transition. (2) The lattice distortion observed in Ce/Zr co-substituted BFO accompanied by the anomalous enhancement of the A1-2 mode induces a magnetic anisotropy in BiFeO_3 . (3) Increasing the Ce/Zr co-substitution decreases the values of crystalline size due to the increase of the compressive stress induced into the BiFeO_3 lattice, while it increases the particle size. (4) The bandgap energy significantly increases with the increasing of Ce/Zr co-substitution suggesting that the materials are suitable as UV and blue-green-driven photocatalysts, or for optoelectronic devices. (5) The weak ferromagnetic behavior observed in Ce/Zr co-substituted samples is related to the following reasons: the destruction of a cycloidal antiferromagnetic structure of BFO due to the rhombohedral-tetragonal structural transition, and the exchange interaction between the 4f- and 3d magnetic orbitals of Ce^{3+} and Fe^{3+} ions.

References

- [1] J.Wang, H. Zheng, V. Nagarajan, B. Liu, S.B. Ogale, D. Viehland, V. Venugopalan, D.G. Schlom, M. Wutting, R. Ramesh, J.B. Neaton, U.V. Waghmare, N.A. Hill, K. M. Rabe, “*Epitaxial BiFeO₃ Multiferroic Thin Film Heterostructures*,” *Science* **299** (2003) 1719–1722.
- [2] D. Lebeugle, D. Colson, A. Forget, and M. Viret, “Very large spontaneous electric polarization in BiFeO₃ single crystals at room temperature and its evolution under cycling fields,” *Appl. Phys. Lett.*, vol. **91**, no. 2, p. 022907, Jul. 2007.
- [3] W. Wei *et al.*, “The magnetoelectric coupling in rhombohedral–tetragonal phases coexisted Bi_{0.84}Ba_{0.20}FeO₃,” *Phys. B Condens. Matter*, vol. 407, no. 12, pp. 2243–2246, Jun. 2012.
- [4] B. Ruetter *et al.*, “Magnetic-field-induced phase transition in BiFeO₃ observed by high-field electron spin resonance: Cycloidal to homogeneous spin order,” *Phys. Rev. B*, vol. 69, no. 6, p. 064114, Feb. 2004.
- [5] A. Mukherjee, S. Basu, L. A. W. Green, N. T. K. Thanh, and M. Pal, “*Enhanced multiferroic properties of Y and Mn codoped multiferroic BiFeO₃ nanoparticles*,” *J. Mater. Sci.*, **50** (2015) 1891–1900.
- [6] Rozhin Irandoust , Ahmad Gholizadeh, “*A comparative study of the effect of the non-magnetic and magnetic trivalent rare-earth ion substitutions on bismuth ferrite properties: Correlation between the crystal structure and physical properties*,” *Solid State Sciences* **101** (2020) 106142.
- [7] Leyla Esmaili, Ahmad Gholizadeh, “*The effect of Nd and Zr co-substitution on structural, magnetic and photocatalytic properties of Bi_{1-x}Nd_xFe_{1-x}Zr_xO₃ nanoparticles*,” *Materials Science in Semiconductor Processing* **118** (2020) 105179.
- [8] Mingqiang Li, Shuzhen Yang, Ruochen Shi, Linglong Li, Ruixue Zhu, Xiaomei Li, Yang Cheng, Xiumei Ma, Jingmin Zhang, Kaihui Liu, Pu Yu, Peng Gao, “*Engineering of multiferroic BiFeO₃ grain boundaries with head-to-head polarization configurations*”, *Science Bulletin*, Available online 29 December 2020 In Press, Corrected Proof,

<https://doi.org/10.1016/j.scib.2020.12.032>.

- [9] Fatemeh Noori and Ahmad Gholizadeh, “*Structural, optical, magnetic properties and visible light photocatalytic activity of BiFeO₃/graphene oxide nanocomposites*”, Mater. Res. Express **6** (2019) 1250g1.
- [10] Xu Jiang, Jie Sun, Xiaojie Chai, Yifan Chen, Wei Zhang, Jun Jiang, Anquan Jiang, “*Large domain-wall current in BiFeO₃ epitaxial thin films*”, Ceramics International Available online 24 December 2020 In Press, Corrected Proof, <https://doi.org/10.1016/j.ceramint.2020.12.161>.
- [11] Pittala Suresh, Binoy Krishna Hazra, B. Ravi Kumar, Tirthankar Chakraborty, P.D. Babud, S. Srinath, “*Lattice effects on the multiferroic characteristics of (La, Ho) co-substituted BiFeO₃*”, Journal of Alloys and Compounds **863** (2021) 158719.
- [12] Mohit Sahni, Sabyasachi Mukhopadhyay, R. M. Mehra, Sunil Chauhan, Prakash Chandra Sati, Manish Kumar, Munendra Singh, Naresh Kumar, “*Effect of Yb/Co co-dopants on surface chemical bonding states of BiFeO₃ nanoparticles with promising photocatalytic performance in dye degradation*”, Journal of Physics and Chemistry of Solids **152** (2021) 109926.
- [13] N.P. Samantray, R.N.P. Choudhary, “*Studies of structural, dielectric and impedance spectroscopy of Ca/Zr modified BiFeO₃ ceramics*”, Materials Chemistry and Physics **260** (2021) 124115.
- [14] Muhammad Akhtar, Sadaf Saba, Saman Arif, Ghulam M. Mustafa, Ayesha Khalid, Ghulam Ali, Shahid Atiq, “*Efficient magnetoelectric dispersion in Ni and Co co-doped BiFeO₃ multiferroics*”, Physica B: Condensed Matter **602** (2021) 412572.
- [15] Rida Ahmed, Ren Jun Si, Sajid ur Rehman, Yi Yu, QiuJu Li, Chunchang Wang, “*High dielectric constant and low temperature ferroelectric-phase-transition in Ca, Pb co-doped BiFeO₃*”, Results in Physics **20** (2021) 103623.
- [16] Yongtao Li, Liqing Liu, Dehao Wang, Hui Zhang, Hongguang Zhang, Xuemin He, QiLi, “*The Local Structure and Exchange Bias Effect of (Ho, Co)-codoped BiFeO₃ investigated by XAFS spectroscopy*”, Physica B: Condensed Matter **604** (2021) 412709.

- [17] Chuang Tian, Qingrong Yao, Zhaofei Tong, Guanghui Rao, Jianqiu Deng, Zhongmin Wang, Jiang Wang, Huaiying Zhou, Jingtai Zhao, “*The influence of Nd substitution on microstructural, magnetic, and microwave absorption properties of BiFeO₃ nanopowders*”, Journal of Alloys and Compounds **859** (2021) 157757.
- [18] D.V. Karpinsky, A. Pakalniškis, G. Niaura, D.V. Zhaludkevich, A.L. Zhaludkevich, S.I. Latushka, M. Silibin, M. Serdechnova, V.M. Garamus, A. Lukowiak, W. Stręk, M. Kaya, R. Skaudžius, A. Kareiva, “*Evolution of the crystal structure and magnetic properties of Sm-doped BiFeO₃ ceramics across the phase boundary region*”, Ceramics International **47** (2021) 5399-5406.
- [19] Ompal Singh, Arun Kumar, Kaushal Kumar, Ashish Agarwal, Sujata Sanghi, “*Sintering time dependent structural and magnetic phase transformations in Pr doped BiFeO₃ multiferroics*”, Journal of Magnetism and Magnetic Materials **519** (2021) 167412.
- [20] A. S. Naeimi, E. Dehghan, D. Sanavi Khoshnoud, and A. Gholizadeh, “*Enhancement of ferromagnetism in Ba and Er co-doped BiFeO₃ nanoparticles*,” J. Magn. Mater., **393** (2015) 502–507.
- [21] Zuci Quan, Hao Hu, Sheng Xu, Wei Liu, Guojia Fang, Meiya Li, Xingzhong Zhao, “*Surface chemical bonding states and ferroelectricity of Ce-doped BiFeO₃ thin films prepared by sol–gel process*”, J. Sol-Gel Sci. Technol., **48** (2008) 261–266.
- [22] Xingmin Zhang, Mei Gao, Yueliang Gu, Hongliang Bao, Xiaolong Li, Xingtai Zhou, and Wen Wen, “*The Structure–Property Investigation of Bi_{1-x}Ce_xFeO₃ (x = 0, 0.05)–Li Battery: In Situ XRD and XANES Studies*”, J. Phys. Chem. C **116** (2012) 20230–20238.
- [23] Jun Liu, Meiya Li, Zhongqiang Hu, Ling Pei, Jing Wang, Xiaolian Liu, Xingzhong Zhao, “*Effects of ion-doping at different sites on multiferroic properties of BiFeO₃ thin films*”, Appl Phys A **102** (2011) 713–717.
- [24] P. C. Sati, M. Kumar, M. Arora, M. Tomar, and V. Gupta, “*Effect of Zr substitution on structural, magnetic, and optical properties of Bi_{0.9}Dy_{0.1}Fe_{1-x}Zr_xO₃ multiferroic ceramics prepared by rapid liquid phase sintering method*,” Ceram. Int., **43** (2017) 4904–4909.
- [25] M. Kumar, M. Arora, S. Chauhan, and S. Joshi, “*Raman spectroscopy probed spin-two*

- phonon coupling and improved magnetic and optical properties in Dy and Zr substituted BiFeO₃ nanoparticles,” J. Alloys Compd.,* **692** (2017) 236–242.
- [26] A. Gholizadeh and N. Tajabor, “*Influence of N₂- and Ar-ambient annealing on the physical properties of SnO₂:Co transparent conducting films,” Mater. Sci. Semicond. Process.,* **13** (2010) 162–166.
- [27] L. Venkidu, M. Veera Gajendra Babu, P. Esther Rubavathi, B. Bagyalakshmi, B. Sundarakannan, “*Structure, microstructure, magnetic and magnetodielectric investigations on BaTi_(1-x-y)Fe_xNb_yO₃ ceramics,”* Ceramics International **44** (2018) 8161–8165.
- [28] Y. Q. JIA, “*Crystal Radii and Effective Ionic Radii of the Rare Earth Ions,”* Journal of Solid State Chemistry **95** (1991) 184–187.
- [29] R.D. Shannon, “*Revised effective ionic radii and systematic studies of interatomic distances in halides and chalcogenides,”* Acta Cryst. A **32** (1976) 751–767.
- [30] A. Gholizadeh, “*A comparative study of physical properties in Fe₃O₄ nanoparticles prepared by coprecipitation and citrate methods,”* J. Am. Ceram. Soc., vol. **100**, no. 8, 2017.
- [31] R. Naik, J. J. Nazarko, C. S. Flattery, U. D. Venkateswaran, V. M. Naik, M. S. Mohammed, G. W. Auner, J. V. Mantese, N. W. Schubring, A. L. Micheli, and A. B. Catalan, “*Temperature dependence of the Raman spectra of polycrystalline Ba_{1-x}Si_xTiO₃,”* Phys. Rev. B **61** (2000) 11367.
- [32] Sunil Chauhan, Manoj Kumar, and Prabir Pal, “*Substitution driven Structural and Magnetic properties and Evidence of Spin Phonon Coupling in Sr-doped BiFeO₃ nanoparticles,”* RSC Adv., 6 (2016) 68028–68040.
- [33] Smita Chaturvedi, Rabindranath Bag, Vasant Sathe, Sulabha Kulkarni and Surjeet Singh, “*Holmium induced enhanced functionality at room temperature and structural phase transition at high temperature in bismuth ferrite nanoparticles,”* J. Mater. Chem. C, **4** (2016) 780–792.

- [34] Mandar M. Shirolkar, Jieni Li, Xiaolei Dong, Ming Li and Haiqian Wang, “Controlling the ferroelectric and resistive switching properties of a BiFeO_3 thin film prepared using sub-5 nm dimension nanoparticles”, *Phys.Chem.Chem.Phys.*, **19** (2017) 26085.
- [35] Jian-Ping Zhou, Rui-Juan Xiao, Yu-Xiang Zhang, Zhenhua Shi and Gang-Qiang Zhu, “Novel behaviors of single-crystalline BiFeO_3 nanorods hydrothermally synthesized under magnetic field”, *J. Mater. Chem. C*, **3** (2015) 6924.
- [36] Yao Wang and Ce-Wen Nan, “Site modification in BiFeO_3 thin films studied by Raman spectroscopy and piezoelectric force microscopy”, *J. Appl. Phys.*, **103** (2008) 114104.
- [37] Manoj K. Singh, Sangwoo Ryu, and Hyun M. Jang, “Polarized Raman scattering of multiferroic BiFeO_3 thin films with pseudo-tetragonal symmetry”, *Phys. Rev. B* **72** (2005) 132101.
- [38] A. Gholizadeh, “The effects of A/B-site substitution on structural, redox and catalytic properties of lanthanum ferrite nanoparticles,” *J. Mater. Res. Technol.*, vol. 8, no. 1, pp. 457–466, Jan. 2019.
- [39] A. Gholizadeh, A. Malekzadeh, and M. Ghiasi, “Structural and magnetic features of $\text{La}_{0.7}\text{Sr}_{0.3}\text{Mn}_{1-x}\text{Co}_x\text{O}_3$ nano-catalysts for ethane combustion and CO oxidation,” *Ceram. Int.*, vol. 42, no. 5, pp. 5707–5717, Apr. 2016.
- [40] A. Gholizadeh, H. Yousefi, A. Malekzadeh, and F. Pourarian, “Calcium and strontium substituted lanthanum manganite–cobaltite [$\text{La}_{1-x}(\text{Ca},\text{Sr})_x\text{Mn}_{0.5}\text{Co}_{0.5}\text{O}_3$] nano-catalysts for low temperature CO oxidation,” *Ceram. Int.*, vol. 42, no. 10, pp. 12055–12063, Aug. 2016.
- [41] W. Zhou, H. Deng, H. Cao, J. He, J. Liu, P. Yang, J. Chu “Effects of Sm and Mn co-doping on structural, optical and magnetic properties of BiFeO_3 films prepared by a sol–gel technique”, *Materials Letters* **144** (2015) 93-96.
- [42] D. Kuang, P. Tang, X. Wu, S. Yang, X. Ding, Y. Zhang, “Structural, optical and magnetic studies of (Y, Co) co-substituted BiFeO_3 thin films”, *Journal of Alloys and Compounds*, **671** (2016) 192-199.
- [43] Jin Li, Xiao Ying Guan, “Structural and optical properties of Ce doped BiFeO_3

- nanoparticles via sol–gel method”, *Micro & Nano Letters*, 2019, Vol. 14, Iss. 13, pp. 1307–1311.
- [44] Jyoti Sharma, Deepak Basandrai, and A K Srivastava, “Ce Co-doped BiFeO₃ multiferroic for optoelectronic and photovoltaic applications”, *Chin. Phys. B* Vol. 26, No. 11 (2017) 116201.
- [45] Zuci Quan, Wei Liu, Hao Hu, Sheng Xu, Bobby Sebo, Guojia Fang, Meiya Li, and Xingzhong Zhao, “Microstructure, electrical and magnetic properties of Ce-doped BiFeO₃ thin films”, *JOURNAL OF APPLIED PHYSICS* **104** (2008) 084106.
- [46] A. Gholizadeh, “A comparative study of the physical properties of Cu-Zn ferrites annealed under different atmospheres and temperatures: Magnetic enhancement of Cu_{0.5}Zn_{0.5}Fe₂O₄ nanoparticles by a reducing atmosphere,” *J. Magn. Magn. Mater.*, vol. 452, pp. 389–397, Apr. 2018.
- [47] A. Gholizadeh and E. Jafari, “Effects of sintering atmosphere and temperature on structural and magnetic properties of Ni-Cu-Zn ferrite nano-particles: Magnetic enhancement by a reducing atmosphere,” *J. Magn. Magn. Mater.*, vol. 422, pp. 328–336, Jan. 2017.
- [48] H. Khedri, A. Gholizadeh, “Experimental comparison of structural, magnetic and elastic properties of M_{0.3}Cu_{0.2}Zn_{0.5}Fe₂O₄ (M = Cu, Mn, Fe, Co, Ni, Mg) nanoparticles” *Applied Physics A: Materials Science and Processing* 125 (2019) 709.
- [49] D. Wang, et al., “Sol–gel synthesis of Nd-doped BiFeO₃ multiferroic and its characterization, *Ceram. Int.* **41** (2015) 8768–8772.
- [50] S. Godara, N. Sinha, B. Kumar, “Study the influence of Nd and Co/Cr co-substitutions on structural, electrical and magnetic properties of BiFeO₃ nanoparticles”, *Ceram. Int.* **42** (1) (2016) 1782–1790.
- [51] T. Wang, T. Xu, S. Gao, S.-H. Song, “Effect of Nd and Nb co-doping on the structural, magnetic and optical properties of multiferroic BiFeO₃ nanoparticles prepared by sol-gel method”, *Ceram. Int.* **43** (2017) 4489–4495.

Figures

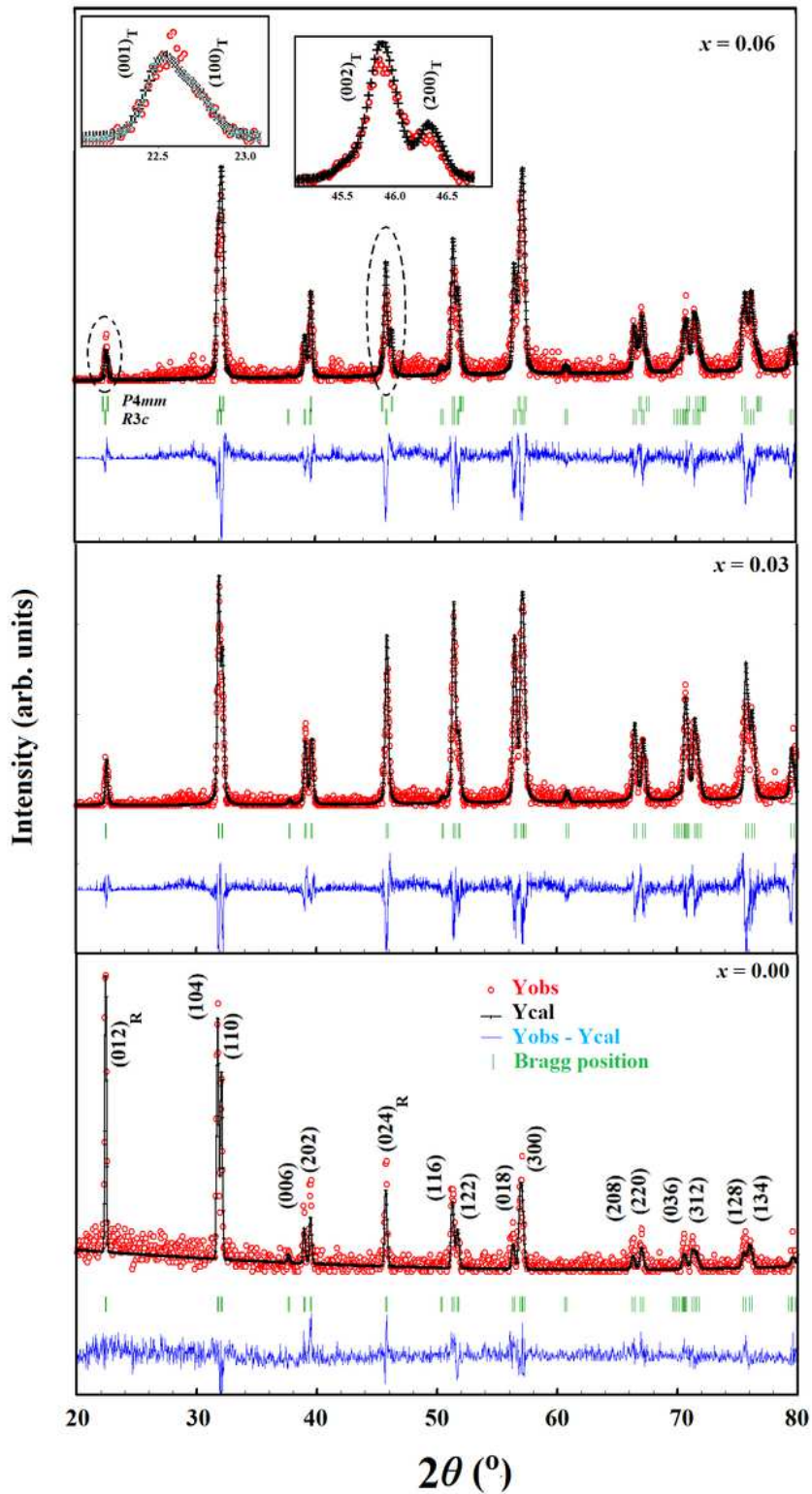


Figure 1

XRD pattern and Rietveld analysis with rhombohedral (space group $R3c$) structural model for $\text{Bi}_{1-x}\text{Ce}_x\text{Fe}_{1-x}\text{Zr}_x\text{O}_3$ ($x = 0.00, 0.03$) and a mixed-phase tetragonal ($P4mm$) + rhombohedral ($R3c$) structural models for $x = 0.06$. Red circles and black solid lines represent the raw data and the calculated profile,

respectively. Green vertical lines indicate the position of Bragg peaks for rhombohedral structure. The blue lower trace shows the difference between the observed (the raw data) and the calculated patterns.

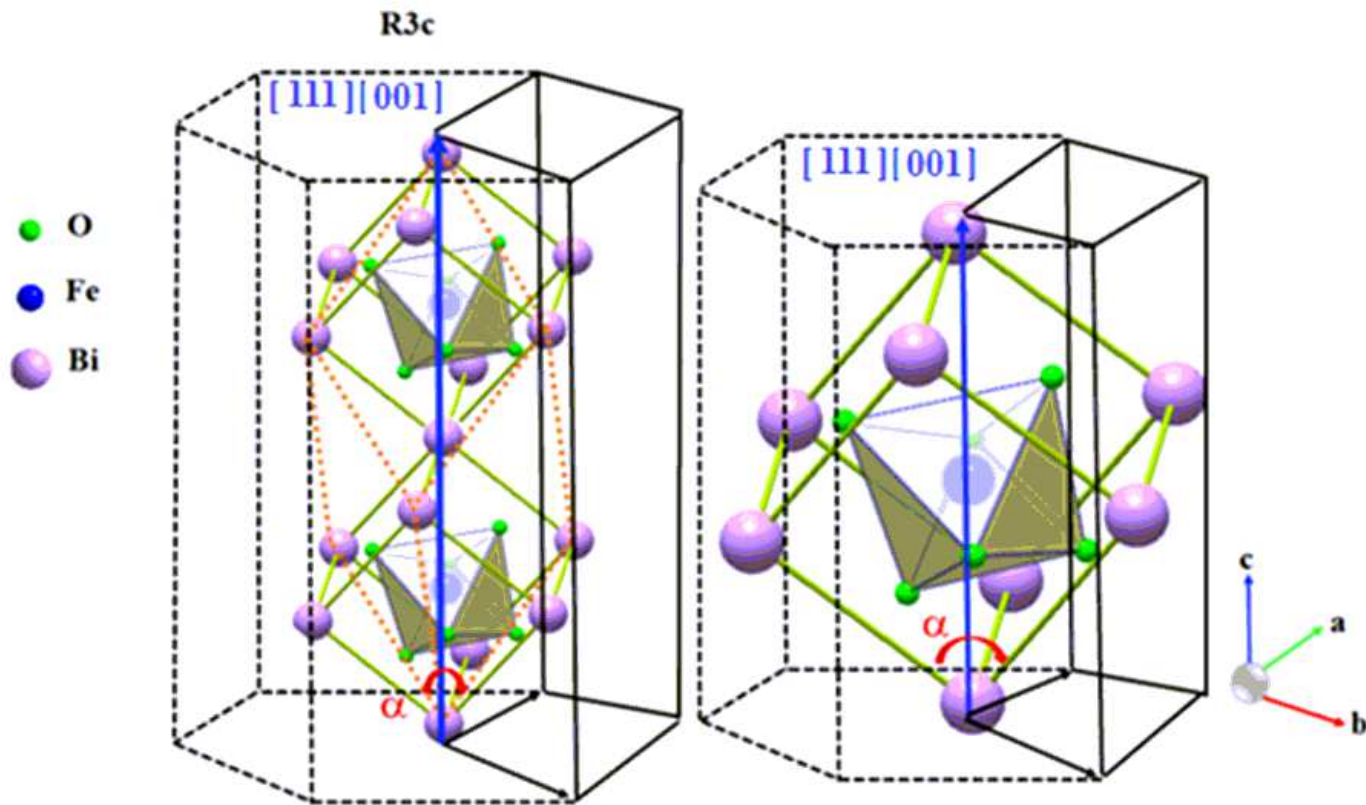


Figure 2

Left panel is a scheme of the relationship between the primitive rhombohedral (dashed, red), cubic (solid, green), and hexagonal cells of bulk BFO. The right panel is half of the left panel. Here, [001] crystallographic axis of the hexagonal structure is parallel to the [111] axis of the rhombohedral or the cubic structures.

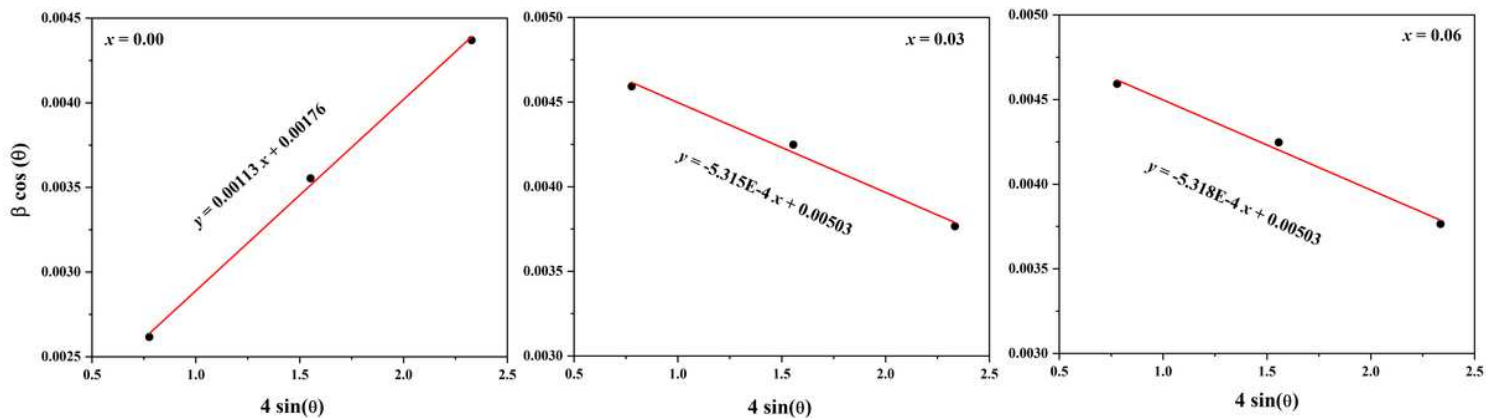


Figure 3

Williamson-Hall plots of $\text{Bi}_{1-x}\text{Ce}_x\text{Fe}_{1-x}\text{Zr}_x\text{O}_3$.

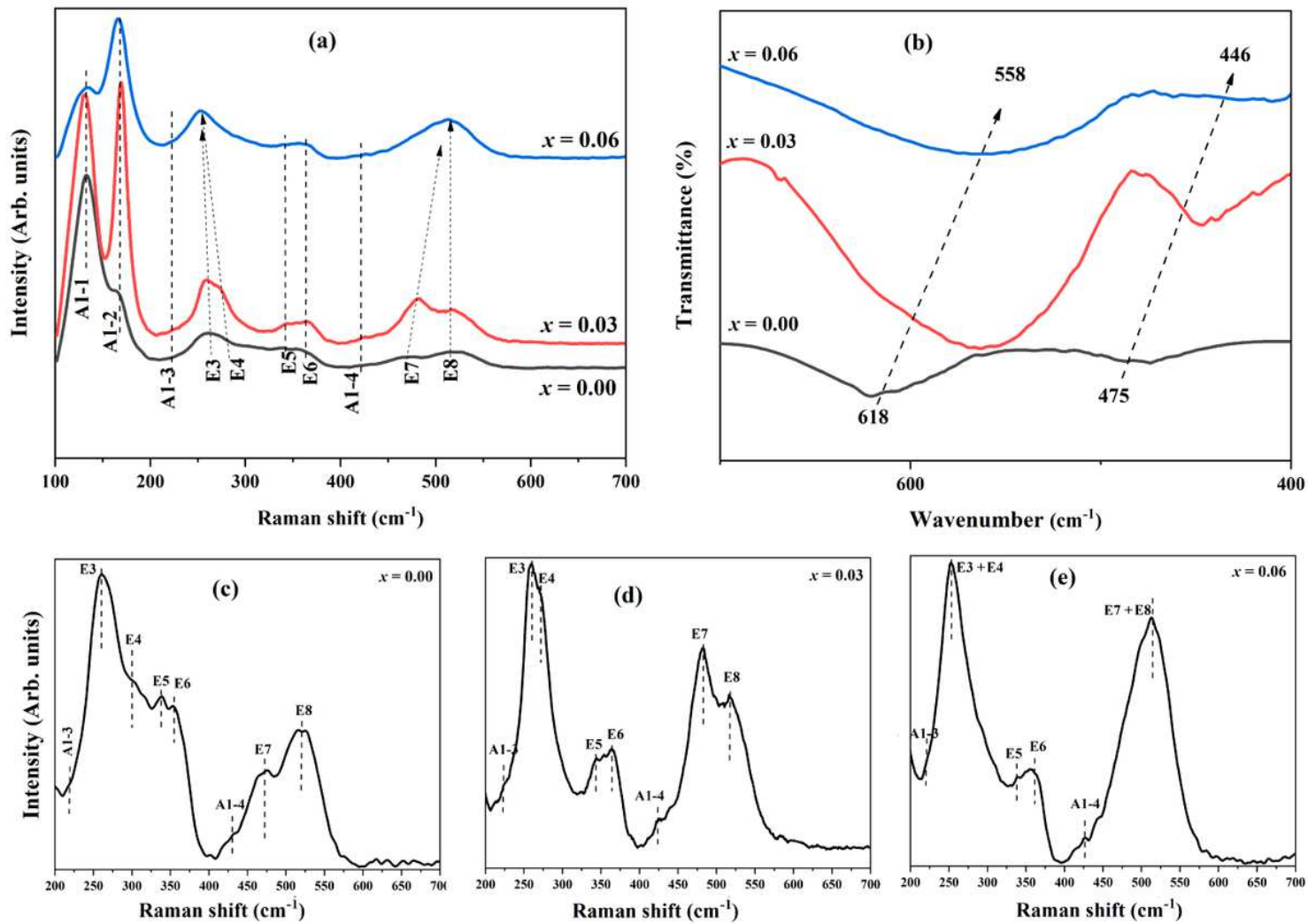


Figure 4

(a) Raman spectra (b) FT-IR spectra of $\text{Bi}_{1-x}\text{Ce}_x\text{Fe}_{1-x}\text{Zr}_x\text{O}_3$. Selected enlarged region (200–700 cm^{-1}) of samples (c) $x = 0.00$, (d) $x = 0.03$, (e) $x = 0.06$.

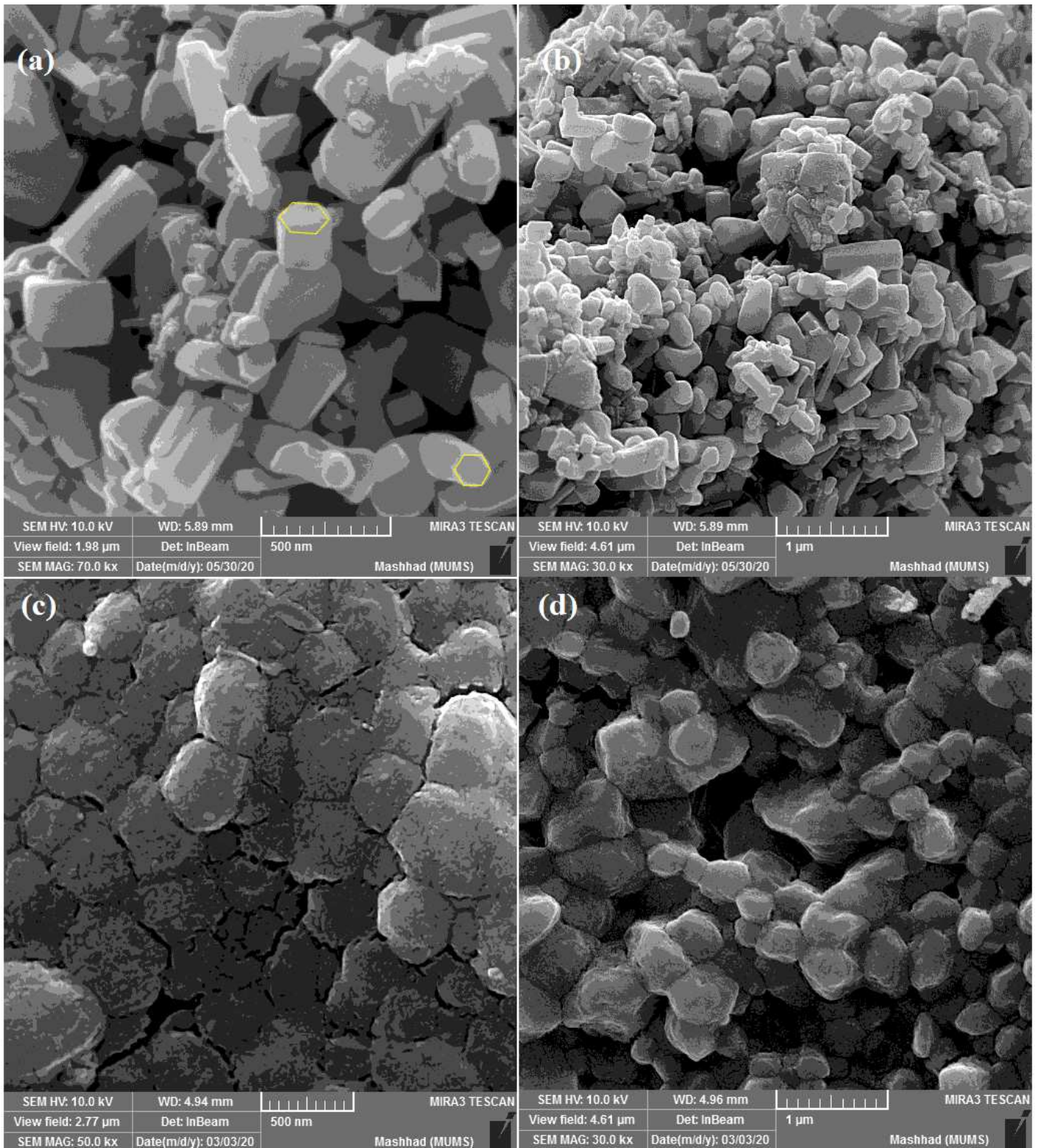


Figure 5

FE-SEM images for (a), (b) $x = 0.00$, and (c), (d) $x = 0.06$ on a scale of 500 nm and 1 μm .

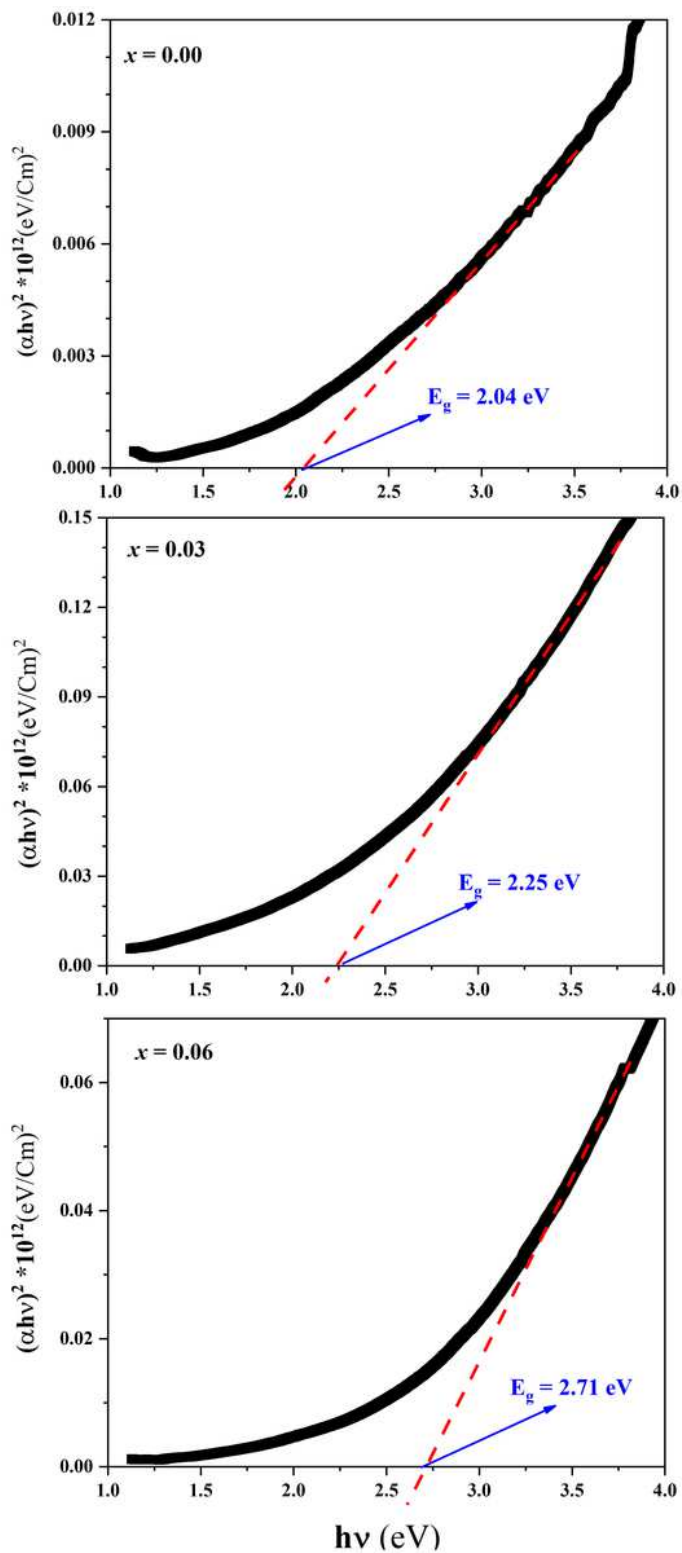


Figure 6

Plots of $(\alpha h\nu)^2$ vs. $h\nu$ for the samples.

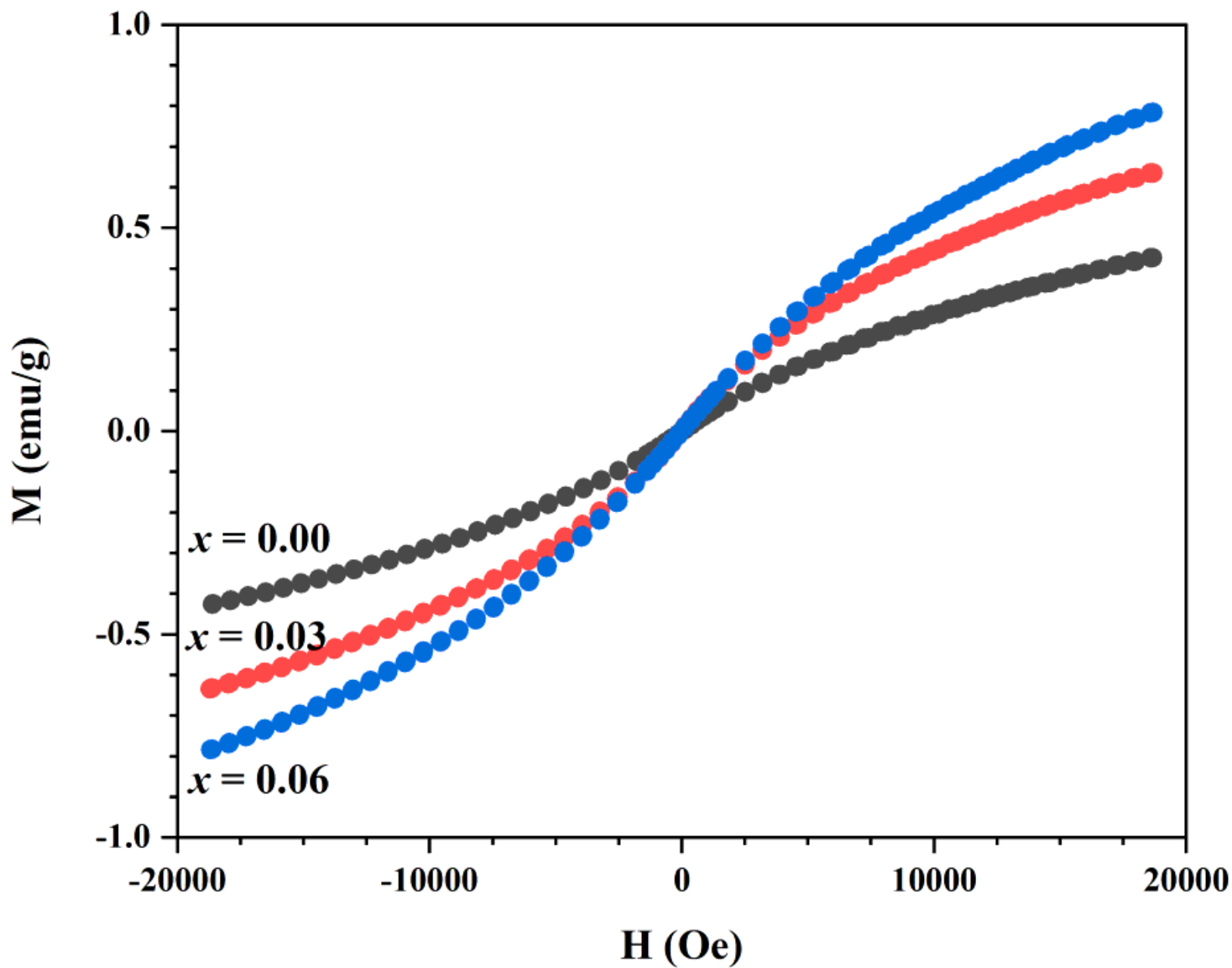


Figure 7

Magnetization curve measured at 300 K for $\text{Bi}_{1-x}\text{Ce}_x\text{Fe}_{1-x}\text{Zr}_x\text{O}_3$.

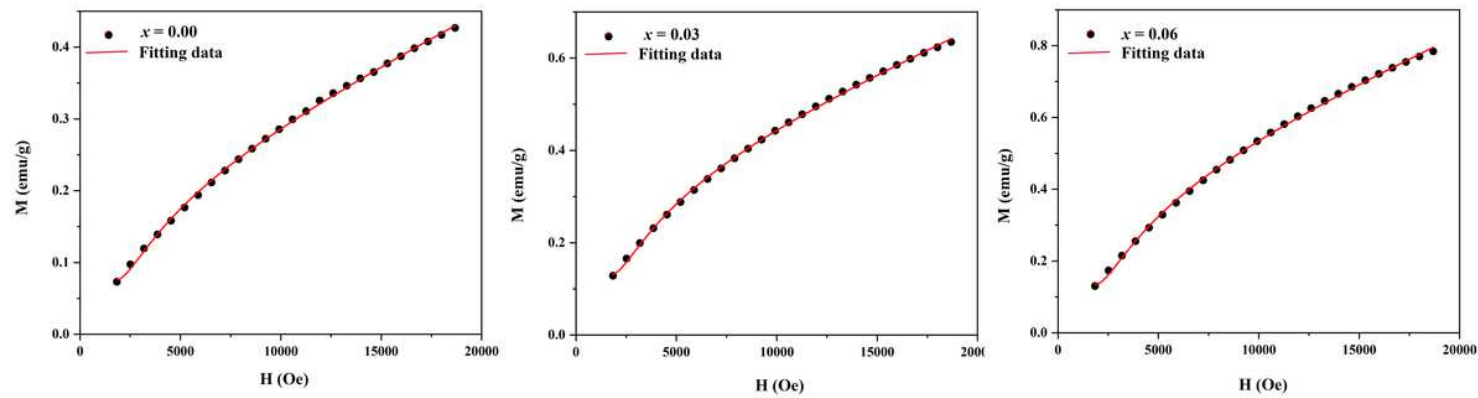


Figure 8

LAS curves for $\text{Bi}_{1-x}\text{Ce}_x\text{Fe}_{1-x}\text{Zr}_x\text{O}_3$.